RSC Advances

ROYAL SOCIETY OF CHEMISTRY

www.rsc.org/advances

Core–shell structured Ag/AgBr@Fe_2O_3 composite was prepared successfully. It has magnetic property, high efficient photocatalytic activity and antibacterial ability.

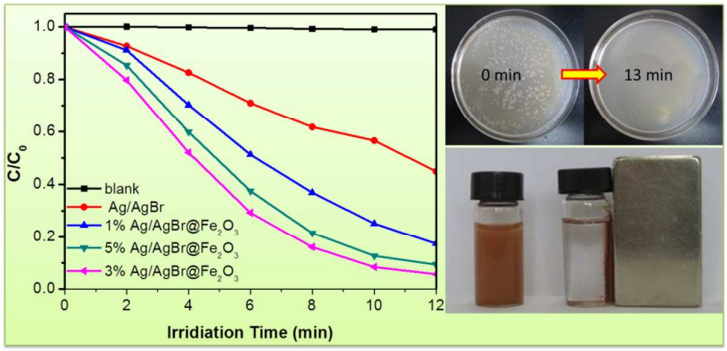

Journal Name

RSCPublishing

ARTICLE

Core–shell structured magnetic Ag/AgBr@Fe_2O_3 composite with enhanced photocatalytic activity for organic pollutants degradation and antibacterium

Cite this: DOI: 10.1039/x0xx00000x

Received 00th January 2012,
Accepted 00th January 2012

DOI: 10.1039/x0xx00000x

www.rsc.org/

Shuquan Huang,[a] Yuanguo Xu,[a] Zhigang Chen,[a] Meng Xie,[a] Hui Xu*,[a] Minqiang He*,[a] Huaming Li[a], Qi Zhang[b]

Core–shell structured magnetic Ag/AgBr@Fe_2O_3 composite was synthesized through a facile solvothermal method. Powder X-ray diffraction (XRD), scanning electron microscope (SEM), X-ray photoelectron spectroscopy (XPS) and ultraviolet-visible absorption spectroscopy (UV-vis) were applied to characterize the structures and properties of as-prepared samples. The results indicate that Fe_2O_3 were coating on the surface of Ag/AgBr and the heterostructures were formed. Electrochemistry analysis and Photoluminescence (PL) spectra analysis indicate the introduction of Fe_2O_3 could improve electron and hole separation efficiency. The photocatalytic activity of the Ag/AgBr@Fe_2O_3 composites were evaluated by using organic dye methyl orange (MO), endocrine disrupting chemical bisphenol A (BPA) and *Escherichia coli (E. coli)* as the target pollutants. The as-prepared Ag/AgBr@Fe_2O_3 composites exhibited much higher photocatalytic activities than pure Ag/AgBr, which was attributed to the effective charge separation of Ag/AgBr@Fe_2O_3 composite. In addition, the as-prepared Ag/AgBr@Fe_2O_3 composite has magnetic ability, after the photocatalytic reaction, it can be quickly separated from solution by an extra magnetic field. Trapping experiments and ESR analysis indicate that the h^+ and $\bullet O_2^-$ are the main active species for the photocatalytic degradation. A possible Z-scheme pathway photocatalytic mechanism was proposed.

Keywords: Core–shell structured, Ag/AgBr, Fe_2O_3, photocatalyst, antibacterial.

Introduction

Recent years, environment issues caused by hazardous wastes and water pollution have been aroused wide concern. Among these, water pollution which is engendered by chemical pollution and pathogrnic microorganisms has been one of the most serious issues in modern society.[1] As a promising technology, semiconductor photocatalysis technique provides a "green" method for environment purification.[2-4] After the discovery of photocatalytic splitting of water on a TiO_2 electrode,[5] plentiful semiconductor materials have been established.[6-13] Among these photocatalysts, plasmonic photocatalysts have been found as an alternative and promising substitute for developing highly efficient visible-light photocatalyst. The plasmonic photocatalysts could dramatically enhance the absorption of visible light and efficiently separate photogenerated electrons and holes because of the surface plasmon resonance (SPR) effect. Generally, noble metal nanoparticles (such as Au and Ag) can photo-induce collective oscillations of the conduction electrons with a resonant frequency, this phenomenon is the surface plasmon resonance (SPR) effect, which can significantly amplify the absorption of visible light.[14] So, the plasmonic photocatalysts provide new opportunities for developing visible light photocatalysts. In recent years, much interest has been paid to the plasmonic photocatalysts based on silver/silver halides (Ag/AgX, X = Cl, Br, I) composite materials due to the surface plasmon resonance (SPR) of noble metallic Ag.[15-21] The silver/silver halides composite photocatalysts have been confirmed that they are not only a photo stable photocatalyst with high visible light photoactivity but also can be used for coupling with other semiconductors to improve the photoactivity. Numerous strategies have been reported for synthesizing Ag/AgX (X = Cl, Br) based photocatalysts, including texturization or morphology control to increase the surface area and band alignment by coupling with other semiconductors. For example, Shen et al.[22] reported that Ag/AgCl spherical and sheetlike nanoarchitecture morphologies could be controllably fabricated by means of

tuning the concentration of CTAC and $AgNO_3$ aqueous solution. The sheet like Ag/AgCl displayed distinctly boosted catalytic performances toward the photodegrdation of methyl orange (MO). Li et al.[23] synthesized 1D AgBr@Ag nanostructures by a facile wet chemical method. These AgBr@Ag nanorods have a high surface area and provide more active sites. Many Ag/AgX based composite photocatalysts have been fabricated, such as $Ag/AgCl/W_{18}O_{49}$, $Ag/AgBr/TiO_2$, and $AgCl@Ag@TiO_2$ etc. These composites not only exhibited very high photocatalytic activity in the photodegrdation of organic pollutant but also show very high antibacterial ability under light irradiation.[24-28] Up to now, this kind of materials has been widely studied in the degradations of non-biodegradable dyes, alcohols, phenols and killing pathogenic bacteria in waste water.[29, 30] However, the practical applications of these photocatalysts are often limited by the easy loss of the suspended particulate catalysts in the process of photocatalytic reaction and separation. So, finding out an easy way to recover the Ag-based photocatalyst is very necessary. To this end, some strategies have been established, one of them is combining Ag/AgX with a magnetic material. For instance, Tian et al.[31] fabricated core–shell structured γ-$Fe_2O_3@SiO_2@AgBr$:Ag composite microspheres. Dai et al.[32] prepared core–shell $Ag–AgI/Fe_3O_4@SiO_2$ plasmonic photocatalyst. An et al.[33] constructed ferromagnetic $Fe_3O_4@SiO_2@AgCl$:Ag plasmonic nanophotocatalysts, etc. These strategies have achieved great advantages in the development of magnetic plasmonic nanophotocatalysts, but the synthesis route could become cumbersome. Our previous work has attempted to construct ferromagnetic plasmonic nanophotocatalysts by coupling Ag/AgCl with magnetic material $CoFe_2O_4$.[34] This synthesis route is simple, but the introduction of $CoFe_2O_4$ leads to the photoactivity of Ag/AgCl decrease. So, it is necessary to continue investigating high efficient magnetic plasmonic nanophotocatalysts for a long and sustained environment protection strategy.

Semiconductor Fe_2O_3, a kind of magnetic material with band gap 2.0-2.2 eV, can absorb a large fraction of visible light.[35] It has lots of advantages in the photocatalytic field, such as environmental-friendly, good chemical stability and low cost.[36] Despite these advantages, Fe_2O_3 suffers from a miserably short excited state lifetime, high recombination rate, poor conductivity and difficulty to separate the photo-induced electron-hole pairs.[37-39] Thus pure Fe_2O_3 may not be a good candidate for photocatalytic reaction. However, as a narrow band gap semiconductor, Fe_2O_3 could be used for modifying other semiconductors to extend the absorb range for visible light, such as Fe_2O_3/TiO_2,[40] Fe_2O_3/ZnO,[41] α - Fe_2O_3/CdS.[42] These results reveal that the introduction of Fe_2O_3 could enhance their photocatalytic abilities. Furthermore, Fe_2O_3 has magnetic property, which provides a new sight for fabricating magnetic photocatalysts. Ye et al.[43] fabricated magnetically separable polymeric carbon nitride photocatalysts Fe_2O_3/g-C_3N_4 and the synergistic effect between Fe_2O_3 and g-C_3N_4 enhanced the photocatalytic activity for the degradation of organic dye under visible light. All in all, these results reveal that the Fe_2O_3 nanoparticles may have potential applications in photocatalysis and magnetic field systems.

Depending on the analysis above, if the hybrid material of Fe_2O_3 and Ag/AgBr is prepared, it is likely that this hybrid structure with higher photocatalytic performance and magnetic property can be obtained. To the best of our knowledge, there are no existing reports on the preparation of such a core–shell structured $Ag/AgBr@Fe_2O_3$ nanoparticle system. In this work, we fabricated magnetic photocatalyst core–shell $Ag/AgBr@Fe_2O_3$ composites by a facile solvothermal method. The as-prepared photocatalyst exhibited excellent photocatalytic activity in eliminating methyl orange (MO), bisphenol A (BPA) and *Escherichia coli (E. coli)* in water under visible light irradiation. This study may provide new insights in the fabrication of high efficient and magnetic plasmonic photocatalysts by a facile method.

Experimental

2.1. Materials

All the reagents were analytical grade and used without further purification. They were purchased from Sinopharm Chemical Reagent Co., Ltd.

2.2. Preparation of photocatalysts

2.2.1. Preparation of Fe_2O_3

Fe_2O_3 was prepared by solvothermal method and followed by calcination method. Firstly, the preparation of Fe_2O_3 precursor: 8.08 g $Fe(NO_3)_3•9H_2O$ was dissolved in 80 mL ethylene glycol under magnetic stirring and then 7.20 g CH_3COONa and 2.00 g polyethylene glycol-600 (PEG-600) were added into the solution and kept stirring for 1.5 h. The result homogeneous suspension was transferred into several 25 mL Teflon-lined autoclaves, followed by solvothermal treatment at 200 ℃ for 22 h. After cooled down naturally, the products were washed three times with pure water and ethanol then dried at 60 ℃ overnight. Secondly, the as-prepared Fe_2O_3 precursor was calcined at air atmosphere at temperature of 500℃ for 2 h.

2.2.2. Synthesis of $Ag/AgBr@Fe_2O_3$ composites

Samples with different mass fraction were synthesized by a facile solvothermal method. In a typical procedure: 100 mL of ethylene glycol (EG) and 100 mL of water were mixed via stirring and ultrasonic processing (solution A). 0.06 g as-prepared Fe_2O_3 was distributed in 15 mL solution A by ultrasonic treatment and then

0.194 g $AgNO_3$ was added under vigorous mechanical stirring for 0.5 h at room temperature to facilitate the adsorption of Ag^+ on the surfaces of the Fe_2O_3 particulates. After that, 1.3 mL potassium bromide solution (the solvent is solution A and the concentration is 0.1 g/mL) was added drop by drop to the above solution and the mixture was keeping stirring for further 30 min in room temperature. At last, the suspension was transferred to 25 mL Teflon-lined stainless-steel autoclaves and kept for 12 h at 140℃. After cooling to room temperature, the precipitate was washed with deionized water and ethanol for three times, and then dried under 60℃ for 12 h. According to this method, different mass fraction of Fe_2O_3 in the total weight of Fe_2O_3 and $AgNO_3$ were 1%, 3%, 5% and 10%, respectively. And the final products were named as 1% Ag/AgBr@Fe_2O_3, 3% Ag/AgBr@Fe_2O_3, 5% Ag/AgBr@Fe_2O_3 and 10% Ag/AgBr@Fe_2O_3, respectively.

2.3 Characterization

The X-ray diffraction (XRD) patterns of the crystal phase was collected on a Bruker D8 diffractometer with high-intensity Cu-Kα (λ = 1.5418 Å) in the 2θ range of 10 –80°.The SEM images of the samples were obtained on a a JEOL-JEM-2010 (JEOL, Japan) operating at 200 kV, which was equipped with an energy-dispersive X-ray spectroscope (EDS) operated at an acceleration voltage of 10 kV. X-ray photoelectron spectroscopy (XPS) was measured on a PHI5300 with a monochromatic Mg Ka source to explore the elements on the surface. The UV–vis diffuse reflectance spectra of the samples were carried out on a Shimadzu UV-2450 UV–vis spectrophotometer (Shimadzu Corporation, Japan) in solid state with the $BaSO_4$ powder was used as the substrate. To diminish the analysis error, a certain amount of samples (about 0.001 g) was mixed with $BaSO_4$ (about 0.009 g), before the UV-vis absorption spectra test. The magnetic properties of the Fe_2O_3 and Ag/AgBr@Fe_2O_3 composites were measured in a vibrating sample magnetometer (Quantum DesignCorporation, USA) with a maximum applied field of ± 2 T. Photocurrent measurements was performed on an electrochemical workstation (CHI 660B, Chenhua Instrument Company, Shanghai, China).

2.4 Photocatalytic activity

The photocatalytic activities of the as-prepared samples were assessed by degrading 10 mg L^{-1} organic dye methyl orange (MO) and 10 mg L^{-1} bisphenol A (BPA) under 300 W Xe lamp with a UV cutoff filter (λ > 420 nm). And all photocatalytic experiments were performed at 30℃ by using a circulating water system to prevent thermal catalytic effects. In addition, an air pump was used to ensure a constant supply of oxygen during the photoreactions. In a typical procedure, 0.07 g as-prepared samples were dispersed in 70 mL above MO or BPA solution. The mixture was magnetically stirred for about 30 min in the dark to ensure the saturated adsorption of organic pollutant on the surface of catalysts. At regular intervals, approximately 4 mL of the suspension was extracted and then centrifuged to remove essentially all the catalysts and the remaining liquid were collected for further test. The remaining MO degradations were analyzed by a UV-vis spectrophotometer (UV-2450, Shimadzu) at wavelength 463 nm. The remaining BPA degradations were analyzed by the two Varian ProStar 210 pumps, an Agilent TC-C18 column, and a Varian ProStar 325 UV-vis Detector at 230 nm. The mobile phase was 1 mL min^{-1} with a solution of methanol and H_2O with the volume ratio 75 : 25 and 20 μL of the sample solution was injected.

2.5 Antibacterial activity

Prior to experiment, all the glassware and the culture medium solution were sterilized by autoclaving at 121℃ for 20 min. And all the experiments were processed under sterile conditions. The antibacterial activities of Ag/AgBr@Fe_2O_3 composites were evaluated by against the *Escherichia coli* (*E. coli*) bacteria. The zone of inhibition test was carried out to identify the antibacterial activities of the prepared photocatalysts in dark. Powder phototcatalysts were placed on the nutrient agar medium which has been inoculated with 20 μL of the prepared *Escherichia coli* (*E. coli*) bacteria suspension. Then the plates were incubated at 37℃ for 16 h in dark.

Photocatalytic disinfection experiments were also performed. In a typical procedure, 10 mg of the as-prepared sample was suspended in 20 mL culture medium solution which contains 1/ (2×10^4) concentration of the original *E. coli* concentration. Then the mixture was magnetically stirred in the dark for 10 min, subsequently, the light was switched on to start irradiation. 20 μL of the solution was sampled at the time intervals of 0 min, 5 min, 10 min and 13 min. Each solution was dispersed on the nutrient agar medium and incubated at 37℃ for 16 h in dark.

Results and discussion

3.1 XRD analysis

The X-ray diffraction (XRD) pattern of AgBr, Fe_2O_3 and Ag/AgBr@Fe_2O_3 composites are shown in Fig.1A. In the patterns of AgBr (Fig.1a), it is obvious that all the diffraction peak at 2θ = 26.7°, 31.0°, 44.3°, 52.5°, 55.0°, 64.5°and 73.2° (marked with "♠") appeared, which matched exactly with the (1 1 1), (2 0 0), (2 2 0), (3 1 1), (2 2 2), (4 0 0) and (4 2 0) crystal planes of cubic phase AgBr (JCPDS No. 06-0438).[44] For the pattern of Fe_2O_3 (Fig.1f), the diffraction peaks at 2θ = 24.2°, 33.2°, 35.6°, 40.9°, 43.3°, 49.5°, 54.1°, 57.6°, 62.5° and 64.1°(marked with "♦") are assigned to the (012), (104), (110), (113), (202), (024), (116), (018), (214) and (300) crystal planes of hematite structure Fe_2O_3 (α-Fe_2O_3) (JCPDS No.33-0664).[45] These peaks at 30.3°, 35.6°, 43.3° and 63.1°(marked with "♣") cannot be ignored in this pattern, they could be indexed to the (220), (311), (400) and (440) crystal planes of cubic phase γ-Fe_2O_3

(JCPDS No.39-1346).[46] This result suggests that the as-prepared Fe_2O_3 contains both hematite structure α-Fe_2O_3 and cubic phase γ-Fe_2O_3. The strong magnetic property of the as-prepared Fe_2O_3 is due to the γ-Fe_2O_3 phase (maghemite). It is difficult to find the peaks of Fe_2O_3 in the patterns of Ag/AgBr@Fe_2O_3 composites, when the mass fraction of Fe_2O_3 is less than 15%. There are two possible reasons, the first one is the peaks of Fe_2O_3 are covered because the peaks of AgBr are very strong. The second one is that the Fe_2O_3 on the surface of AgBr are well dispersed. Similar result can also be found in other systems.[47] However, we magnified the patterns of 1% Ag/AgBr@Fe_2O_3, 3% Ag/AgBr@Fe_2O_3 and 5% Ag/AgBr@Fe_2O_3 samples by narrow-scan diffraction patterns, as showed in Fig.1B, the peaks of Fe_2O_3 still could not be noticed. So, we believe the second one is the main reason and this conjecture has also been confirmed by the followed SEM, EDS and XPS analysis.

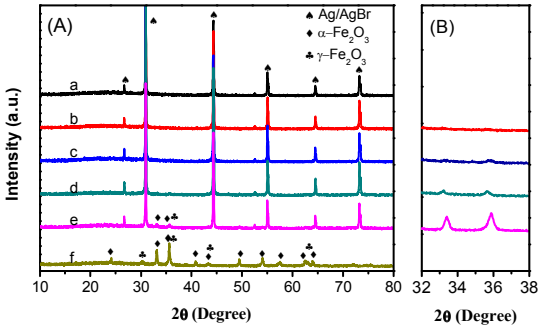

Fig.1 XRD patterns of the as-prepared photocatalysts series. (A) wide-scan diffraction patterns: a. pure Ag/AgBr, b. 1% Ag/AgBr@Fe_2O_3, c. 3% Ag/AgBr@Fe_2O_3, d. 5% Ag/AgBr@Fe_2O_3, e. 15% Ag/AgBr@Fe_2O_3 and f. Fe_2O_3. (B) narrow-scan diffraction patterns.

3.2 SEM and EDS analysis

Fig. 2 shows the morphology of Ag/AgBr and the dispersion state of Fe_2O_3 on the surface of Ag/AgBr, which were examined by scanning electron microscopy (SEM). Fig. 2a–b are the morphology image of pure Fe_2O_3, it can be seen that the Fe_2O_3 particles are granular like with diameters of ca. 20-50 nm. Fig. 2c shows the morphology image of pure Ag/AgBr, the large particles with diameters of ca. 7-15 μm are AgBr particles and some of the small particles attached on their surface are Ag NPs.[48] By close observation (Fig. 2d), these Ag NPs are scattering on the surface of AgBr sparsely. This may be the reason why the peaks of Ag^0 couldn't be found in the XRD patterns. Fig. 2e–f are low and high magnification SEM images of 1% Ag/AgBr@Fe_2O_3 composites, respectively. In the low magnification SEM image, it can be seen that the introduction of Fe_2O_3 didn't change the shape of Ag/AgBr largely, while in high magnification SEM image (Fig. 2f), it can be clearly seen that Fe_2O_3 NPs were highly distributed throughout the surface of Ag/AgBr. Similarly, the SEM images of 3% Ag/AgBr@Fe_2O_3 and 5% Ag/AgBr@Fe_2O_3 are shown in Fig. 2g–h and Fig. 2i–j, respectively. It can be seen that with the increase of Fe_2O_3 content more and more holes can be found on the surface of Ag/AgBr, indicating that some of the Fe_2O_3 are wrapped inside of AgBr particles. Similar results can also be found in our previous work.[49] In addition, it can be noticed that an agglomeration of Fe_2O_3 particle was formed when the content of Fe_2O_3 in a high level (>3%), this may decrease the photocatalytic activity of Ag/AgBr@Fe_2O_3 composites. At the same time, energy-dispersive X-ray spectroscope (EDS) of pure Ag/AgBr and 3% Ag/AgBr@Fe_2O_3 have also been taken out and shown in Fig. 2k–l, respectively. Only Ag and Br can be found in the image of Ag/AgBr, while in the image of 3% Ag/AgBr@Fe_2O_3 composites Ag, Br, Fe and O were directly observed. Combining the results of XRD, SEM and EDS, it can be confirmed that Ag/AgBr@Fe_2O_3 has been successfully synthesized.

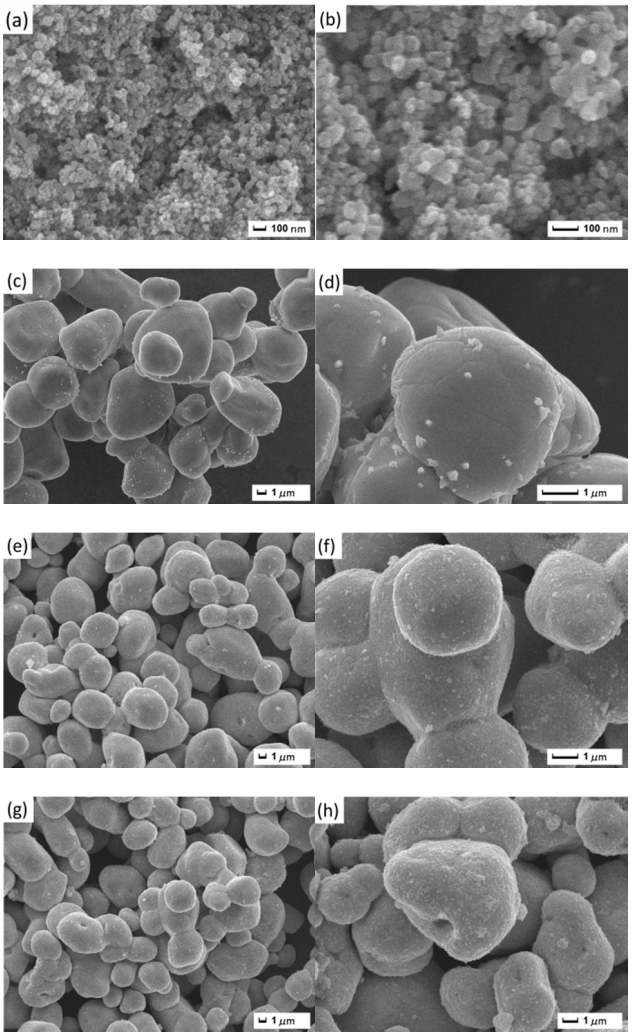

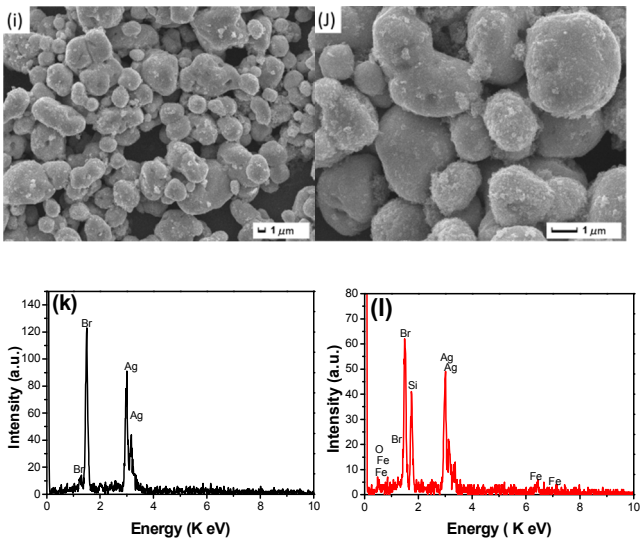

Fig. 2 Low and high magnification SEM images of of as-prepared samples: Fe2O3 (a–b), Ag/AgBr (c–d), 1% Ag/AgBr@Fe_2O_3 (e–f), 3% Ag/AgBr@Fe_2O_3 (g–h), 5% Ag/AgBr@Fe_2O_3 (i–j), EDS of Ag/AgBr (k) and 3% Ag/AgBr@Fe_2O_3 (l).

3.3 XPS analysis

X-ray photoelectron spectroscopy (XPS) analysis was carried out to further determine the elemental compositions and chemical status of the as-prepared Ag/AgBr and Ag/AgBr@Fe_2O_3 composite. The results were shown in Fig. 3. The full scan survey XPS spectrum of the Ag/AgBr and 3% Ag/AgBr@Fe_2O_3 composite indicate that the product consists of Ag, Br, Fe, O and C elements (Fig. 3a). The C element is from the XPS instrument itself. Fig.3b shows the high-resolution XPS spectrum of Ag 3d, it consists two individual peaks at about 366.00~367.00 eV and 372.00~373.00 eV, which are attributed to Ag $3d_{5/2}$ and Ag $3d_{3/2}$ binding energies, respectively.[50] In contrast to Ag/AgBr, the Ag 3d spectra of Ag/AgBr@Fe_2O_3 composite show a little shift, the decrease in the binding energy with an amount of ~0.4 eV might be attributed to the interaction of Ag^+ ions of the composite with the Fe_2O_3 nanoparticles. It also suggests that the interaction between Fe_2O_3 and Ag/AgBr existed and the combination sites are Ag elements.[51,80] The spectra of Br 3d are shown in Fig. 3c. The binding energies of Br $3d_{5/2}$ and Br $3d_{3/2}$ are about 67.69 eV and 68.58 eV, respectively, which can be attributed to the Br atoms existing in a Br^- state.[52] In addition, it is worth noting that both the intensity of Ag 3d and Br 3d of Ag/AgBr@Fe_2O_3 composite are much weaker than that of Ag/AgBr, respectively. Considering that the main components of the composites are Ag/AgBr, this result confirmed that the Fe_2O_3 NPs were covered on the surface of Ag/AgBr again. Fig. 3d shows the spectra of Fe 2p, the two peaks at about 710.54 eV and 724.15 eV are attributed to the binding energies of Fe $2p_{3/2}$ and Fe $2p_{1/2}$, respectively. The high-resolution O 1s XPS spectra of Ag/AgBr and Ag/AgBr@Fe_2O_3 samples are shown in Fig. 3e, The peak at about 529.71 eV can be assigned to the oxygen in Fe_2O_3 crystals,[53] and the peak at about 531.52 eV is considered to be the enthetic O, such as ambient adsorption.[54]

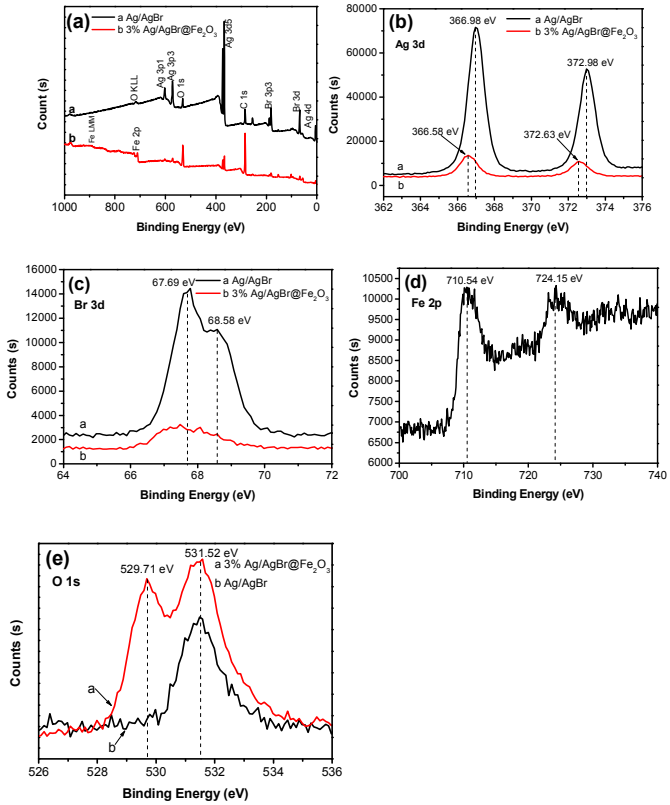

Fig. 3 XPS spectra of the pure Ag/AgBr and 3% Ag/AgBr@Fe_2O_3 composite. (a) Survey of the sample; (b) Ag 3d; (c) Br 3d; (d) Fe 2p and (e) O 1s.

3.4 UV-vis absorption spectra analysis

Fig. 4 shows the UV-vis absorption spectra (in the diffuse reflectance spectra mode) and corresponding Tauc's plots of $(\alpha h\nu)^2$ vs ($h\nu$) of as-prepared samples.[55] From the UV-vis absorption spectra (Fig. 4a), it can be seen that the bare Ag/AgBr has a main absorption region from 200 to 450 nm. And the absorption in the range 500−700 nm is ascribed to the SPR effect of Ag nanoparticles on the surface of the AgBr, which indicates the existence of Ag^0 in the composite catalysts. This result is in accordance with our previous work.[48] For the Ag/AgBr@Fe_2O_3 composites, an apparent absorption enhancement for light is observed compared to the pure Ag/AgBr, which is thought to result from Ag/AgBr covered by Fe_2O_3. This result is consistent with the SEM and XPS analysis above. Furthermore, the light absorption ability was enhanced with the increased Fe_2O_3 contents. The enhanced light absorption may lead to forming more electron–hole pairs.[56] In addition, It shouldn't be neglected that the light absorption ability of pure Fe_2O_3 is less than that of Ag/AgBr@Fe_2O_3 composites in the range 600 – 800 nm, which suggests a synergistic effect between Ag/AgBr and Fe_2O_3.[57]

The band gap energy Eg of the as-prepared Fe_2O_3 and Ag/AgBr was estimated from the corresponding Tauc's plots of $(\alpha h\nu)^2$ vs $(h\nu)$,[54] and the result is shown in the Fig. 4b. The band gap energy of as-prepared Fe_2O_3 and Ag/AgBr was estimated to be 2.1 eV and 2.6 eV, respectively, which is similar to the reported literatures.[58,51] In addition, to study the flowchart of photo-excited charge carriers, potentials of the conduction band (CB) and valence band (VB) edges of as-prepared Fe_2O_3 was evaluated by Mulliken electronegativity theory: $E_{CB}= X - E_C - 0.5(Eg)$, where X was the absolute electronegativity of the atom semiconductor, E_C was the energy of free electrons with the hydrogen scale (4.5 eV); Eg was the band gap of the semiconductor. Therefore, the conduction band (CB) of Fe_2O_3 and AgBr was determined to be 0.3 eV and 0 eV, respectively, which are similar to the reported literatures.[59,60] Then the valence band (VB) can be determined by $E_{VB}= E_{CB} + Eg$, and the values are 2.4 eV and 2.6 eV for Fe_2O_3 and AgBr, respectively.

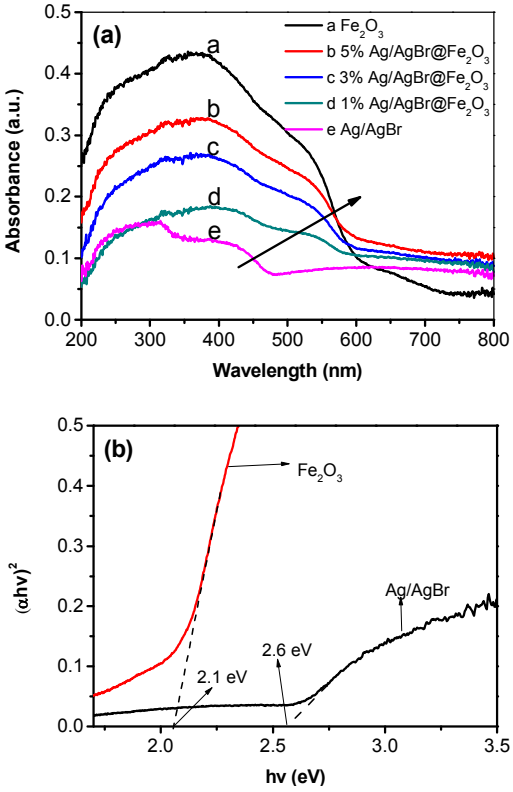

Fig. 4 (a) UV-vis absorption spectra of as-prepared samples and (b) corresponding Tauc's plots of $(\alpha h\nu)^2$ vs $(h\nu)$ of Fe_2O_3 and Ag/AgBr.

3.5 Electrochemistry analysis

It is widely accepted that the higher photocurrent was, the better electron and hole separation efficiency would be.[62,63] Fig. 5 shows 5 on−off cycles visible light irradiation transient photocurrent responses of Ag/AgBr and 3% Ag/AgBr@Fe_2O_3 hybrid material. Obviously, the 3% Ag/AgBr@Fe_2O_3 hybrid material have higher photocurrent response than that of the Ag/AgBr. It indicates that the 3% Ag/AgBr@Fe_2O_3 hybrid material has a higher separation rate of photoexcited electrons and holes under the irradiation of visible light.[64, 65] In addition, it can be seen that the photocurrent value rapidly decreased and increased to a constant value when the light was off and on. This result demonstrated that the recombination of electrons and holes was inhibited greatly, which is good for photocatalytic reaction.[66]

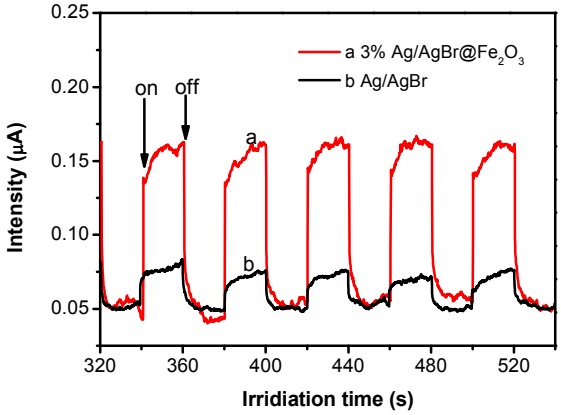

Fig. 5 Transient photocurrent response for pure Ag/AgBr and 3% Ag/AgBr@Fe_2O_3 composite.

3.6 PL analysis

To further confirm that the introduction of Fe_2O_3 could reduce the electrons and holes recombination rate. Photoluminescence (PL) spectra for Ag/AgBr and 3% Ag/AgBr@Fe_2O_3 hybrid material were presented in Fig. 6. It is obvious that PL intensity of 3% Ag/AgBr@Fe_2O_3 decreased significantly compared to that of Ag/AgBr, which means efficient transfer of photoexcited electrons between Fe_2O_3 and Ag/AgBr. This result indicates that the introduction of Fe_2O_3 favors the effective charge separation of Ag/AgBr and improve the photocatalytic activities.[67]

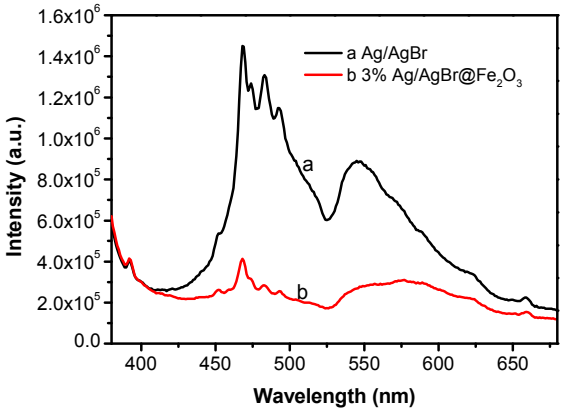

Fig. 6 PL spectra of pure Ag/AgBr and 3% Ag/AgBr@Fe_2O_3 composite.

3.7 VSM analysis

Fig. 7 shows the magnetic behavior of as-prepared Fe_2O_3 and 3% Ag/AgBr@Fe_2O_3 composite, which is investigated by a vibrating sample magnetometer at room temperature. The curve presents almost no hysteresis loop, which suggests that the as-prepared Fe_2O_3 and 3% Ag/AgBr@Fe_2O_3 composite have ferromagnetic behavior.[68] The magnetization saturation (*M*s) values are 34.9 and 3.3 emu/g for Fe_2O_3 and 3% Ag/AgBr@Fe_2O_3 composite, respectively. The magnetic separation ability of the 3% Ag/AgBr@Fe_2O_3 composite was tested in water by placing a magnet near the glass bottle. The red particles were attracted toward the magnet within a short time (Figure 6 inset graph). Therefore, this will provide an easy and efficient way to separate the photocatalysts from water under an external magnetic field.

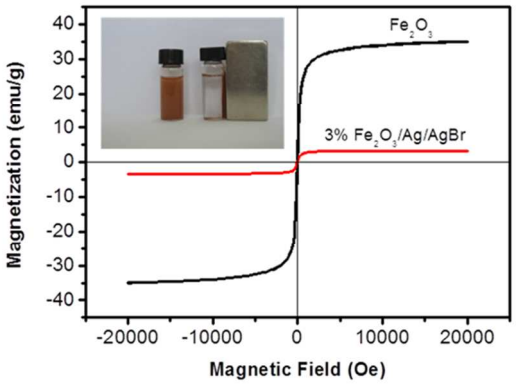

Fig.7 The hysteresis loops of pure Fe_2O_3 and 3% Ag/AgBr@Fe_2O_3 composite (the inset graph shows the sample dispersed in water (left) and separated by external magnet (right)).

3.8 Photocatalytic activity

Photodegradation of MO under visible light irradiation was carried out to evaluate the photocatalytic ability of the as-prepared samples. As shown in Fig. 8a, it can be seen that MO self-decomposition is negligible. The pure Ag/AgBr could degrade MO by 55.1% after 12 min under visible light irradiation. The Ag/AgBr@Fe_2O_3 composites show much better photocatalytic activity than Ag/AgBr alone. After visible light irradiation for 12 min, the degradation efficiency of MO over 1% Ag/AgBr@Fe_2O_3, 3% Ag/AgBr@Fe_2O_3 and 5% Ag/AgBr@Fe_2O_3 are 91.7%, 94.4% and 82.7%, respectively. It can be noticed that the photocatalytic ability of Ag/AgBr@Fe_2O_3 composites is greatly influenced by the content of Fe_2O_3. When the Fe_2O_3 content is 3%, it has the best photocatalytic activity. Whatever the Fe_2O_3 content is high or less than 3% (such as 1% and 5%), its photocatalytic activity decreased. This result is consistent with the SEM analysis. The linear relationship of $-\ln(C_0/C)$ *versus* time is shown in Fig. 8b and the pseudo-first-order constants and relative coefficients are summarized in Table 1. The results indicate that the photocatalytic activity was improved by the introduction of Fe_2O_3 compared to pure Ag/AgBr. Especially, the 3% Ag/AgBr@Fe_2O_3 composite exhibit about 3.35 times degradation rate as high as that of pure Ag/AgBr. Fig. 8c shows the time-dependent absorption spectra of MO solution in the presence of 3% Ag/AgBr@Fe_2O_3 composite. It can be seen that the color of MO solution changed from yellow to light yellow and then colourless during the reaction (Fig. 8c inset graph). An evident decrease in MO absorption at λ = 463 nm was observed, indicating that the chromophoric structure was destroyed.

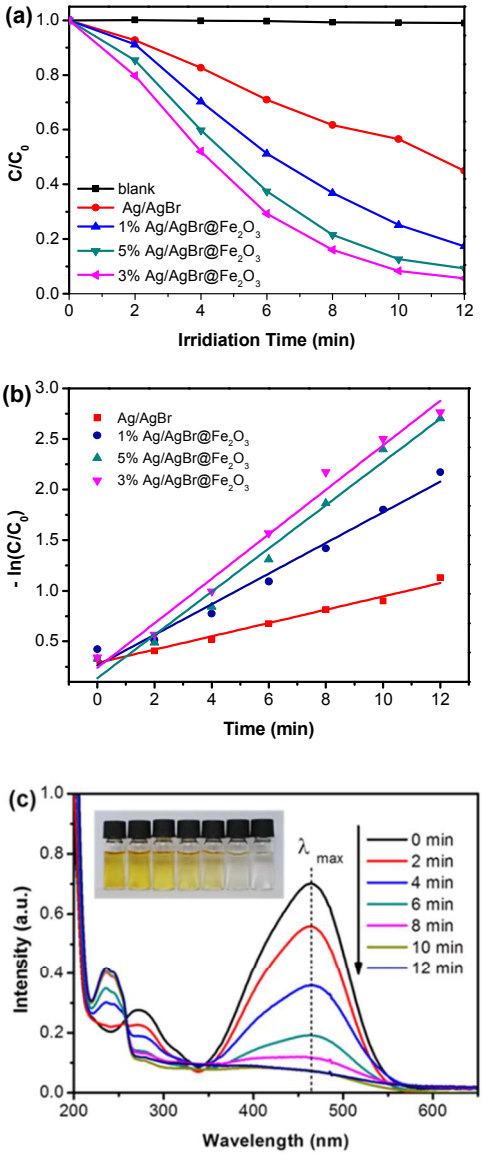

Fig. 8 (a) Photodegradation of MO by as-prepared samples. (b) time-dependent absorption spectra of MO solution in the presence of 3% Ag/AgBr@Fe_2O_3 composite.

Table 1 Kinetic constants and regression coefficients of MO degradation under visible-light irradiation.

Sample	Kinetic constant (k, min^{-1})	R^2
Ag/AgBr	0.06571	0.98061
1% Ag/AgBr@ Fe_2O_3	0.15124	0.97464
5% Ag/AgBr@ Fe_2O_3	0.21371	0.97861
3% Ag/AgBr@ Fe_2O_3	0.21991	0.98140

Bisphenol-A (2, 2-bis (4-hydroxyphenyl) propane, BPA), which is a compounds termed endocrine disruptor, has frequently been detected in surface water due to it is widely used in the production of polycarbonate plastics and epoxy resins. The toxicity tests revealed that it may cause various adverse effects on aquatic organisms even at low exposure levels.[69] Therefore, the degradation of BPA is important. In this work, the degradation of BPA under visible light with the as-prepared samples also has been studied. The remaining BPA degradations were analyzed by a UV-vis spectrophotometer (UV-2450, Shimadzu) at wavelength 230 nm. As shown in Fig. 9a, it can be seen that the BPA couldn't self-decomposition without catalysts. The pure Ag/AgBr has very low degradation rates for BPA, only 26.0% BPA were degraded within 3h. While the Ag/AgBr@Fe_2O_3 composites exhibit a relative higher photodegradation for BPA, as same as the photodegradation for MO, the 3% Ag/AgBr@Fe_2O_3 composite exhibit the best photocatalytic activity, it can degrade BPA up to 69.0% within 3h. The HPLC analysis of BPA solution in the presence of 3% Ag/AgBr@Fe_2O_3 composite has been taken out. The results showed in Fig. 9b, it is obvious that the characteristic peak of BPA decreased with the photoreaction process, which confirmed that BPA was indeed degraded by 3% Ag/AgBr@Fe_2O_3 composite.

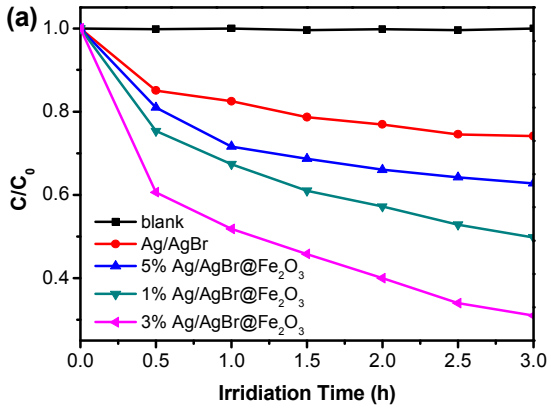

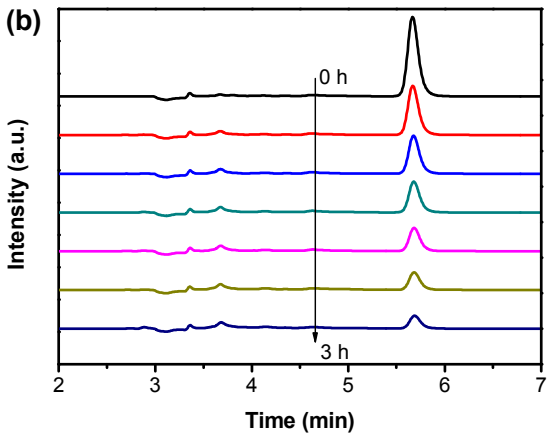

Fig. 9 (a) Photodegradation of BPA by as-prepared samples. (b) The HPLC of the BPA degraded solution for different times in the presence of 3% Ag/AgBr@Fe_2O_3.

3.9 Photocatalytic antibacterial activity

Fig. 10a shows the results of the antibacterial experiment of 3% Ag/AgBr@Fe_2O_3 in the dark. It is obvious that the 3% Ag/AgBr@Fe_2O_3 composite has a clear inhibition zone of about 16 mm against *E. coli*. This result indicates 3% Ag/AgBr@Fe_2O_3 has a good antibacterial ability in the dark. Fig. 10b shows the results of the photocatalytic antibacterial experiments. It can be seen that the amount of *E. coli* was not obviously decrease under the visible light irradiation, indicating that the *E. coli* could survive under visible light irradiation. In the presence of 3% Ag/AgBr@Fe_2O_3 composite, numerous *E. coli* were still alive without light irradiation. However, when the system was irradiated by visible light for 5 min, more than half of the *E. coli* were killed. When the system was irradiated for 10 min, only a small number of *E. coli* were survived. When the system was irradiated for 13 min all the *E. coli* were killed. This result indicates that 3% Ag/AgBr@Fe_2O_3 possesses antibacterial ability under visible light irradiation.

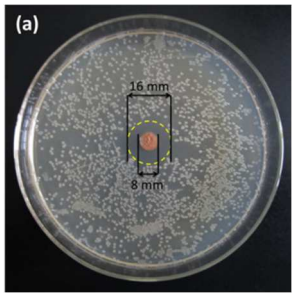

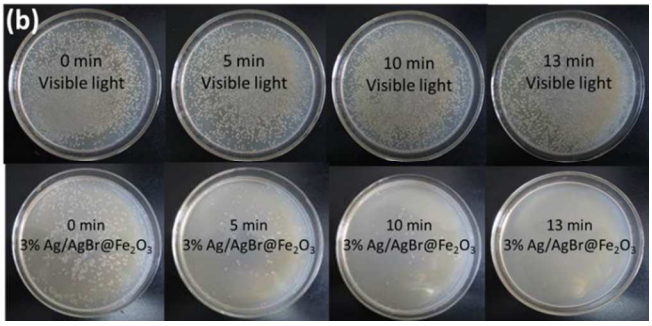

Fig. 10 The representative inhibition zone of 3% Ag/AgBr@Fe_2O_3 disks against *E. coli* after 16 h incubation in the dark (a) and the photocatalytic antibacterial activities of light only and 3% Ag/AgBr@Fe_2O_3 against E. coli at different irradiation times (b).

3. 10 Cycling runs

The recycle ability of magnetic photocatalyst is an important property for practical applications. To evaluate the reusability of the Ag/AgBr@Fe_2O_3 hybrid material, recycling reactions for degrading MO over 3% Ag/AgBr@Fe_2O_3 under visible light were carried out. As shown in Fig. 11, the MO still can be degraded up to 89.1% after five consecutive cycles, which implies the high recycle ability of Ag/AgBr@Fe_2O_3 hybrid material.

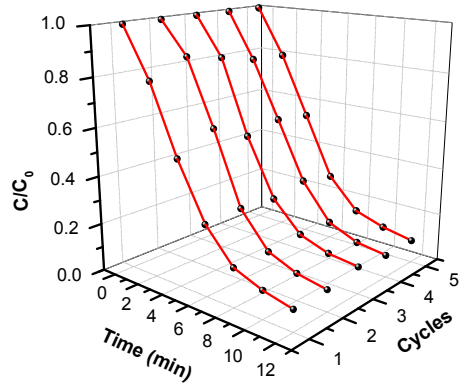

Fig. 11 Cycling runs of 3% Ag/AgBr@Fe_2O_3 composite.

3.11 Mechanism of pollutant photodegradation

To study the photodegradation mechanism, the trapping experiments of active species were taken out by using 2-propanol as the hydroxyl radical (•OH) scavenger, N_2–bubbling for inhibiting the superoxide radical ($•O_2^-$), and triethanolamine (TEOA) as the hole (h^+) radical scavenger.[70] The results are shown in Fig. 12. It can be seen that the degradation rate of MO was hardly affected by adding 1mM 2-propanol, indicating that the •OH is not the main reactive species. The degradation rate of MO was decreased under an N_2 atmosphere, suggesting that the $•O_2^-$ plays an important role in photodegradation process. When 1mM TEOA was added, the degradation rate of MO was greatly inhibited, which reveals that the h^+ was a dominant reactive species. To further confirm the active species in the photodegradation process, the electron spin resonance (ESR) spin-trap technique were carried out. The Ag/AgBr and 3% Ag/AgBr@Fe_2O_3 composite were dispersed with DMPO in water and irradiated for 8 min by a Quanta-Ray Nd:YAG pulsed laser system, and the results are shown in Fig.13. Under visible light irradiation, the characteristic signals of both the DMPO-superoxide radical ($•O_2^-$) and the DMPO-hydroxyl radical (•OH) could be observed. In addition, it is obviously that the signal intensity of the 3% Ag/AgBr@Fe_2O_3 is much higher than that of Ag/AgBr for both the DMPO-superoxide radical ($•O_2^-$) and the DMPO-hydroxyl radical (•OH). This result reveals a synergistic effect between AgBr and Fe_2O_3, which could enhance the formation of reactive species thus improve photocatalytic performance. The ESR analysis indicate that the $•O_2^-$ and •OH are formed, this result is a little different from the trapping experiments result. Both ESR analysis and trapping experiments revealed $•O_2^-$ plays an important role in photodegradation process, but it is very different for •OH. Trapping experiments revealed •OH did not affect the degradation rate of MO, however, ESR analysis revealed the characteristic signals of DMPO-hydroxyl radical (•OH). It is well known that the •OH could oxide MO in solution.[71,72] So, if the •OH is actually formed in the MO degradation process, the trapping experiment of •OH will reveal according result (the degradation rate of MO was affected more or less by adding 1mM 2-propanol), but in fact it didn't. Considering that the ESR experiments and the trapping experiments were performed under different solutions, suggesting the •OH did not formed in the MO degradation process. It is well known that photocatalyst adsorption ability for dye also play a critical role in the photo-degradation process. Fig. 14 shows the comparison of MO adsorption ability of pure Ag/AgBr and 3% Ag/AgBr@Fe_2O_3 composite in 15 min. It can be seen that at a same origin MO concentration, the MO adsorption ability of 3% Ag/AgBr@Fe_2O_3 composite is much higher than that of pure Ag/AgBr. Therefore, an adsorption oxidation mechanism was proposed, as discussed below.

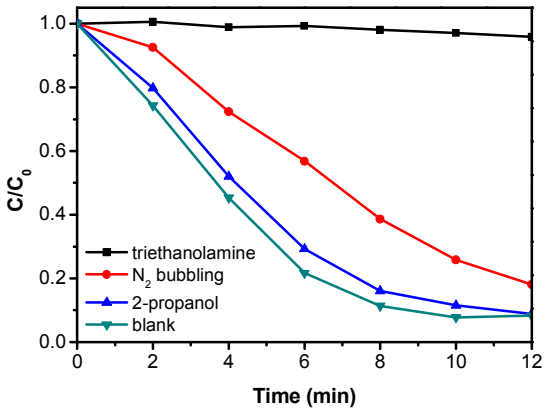

Fig. 12 Trapping experiments of active species in the photocatalytic process.

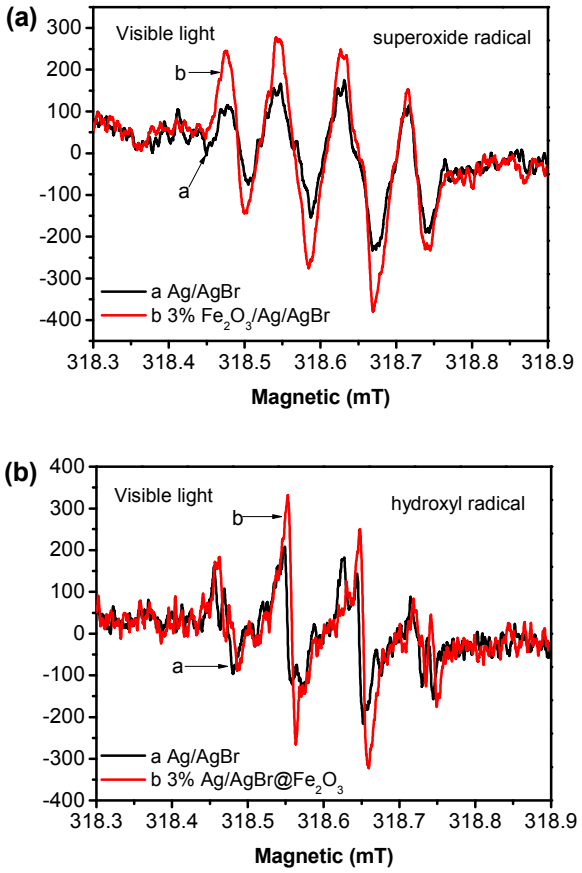

Fig. 13 ESR spectra of radical adducts trapped by DMPO in Ag/AgBr and 3% Ag/AgBr@Fe_2O_3 composite aqueous dispersion under visible light irradiation. ESR spectra of (a) superoxide radical and (b) hydroxyl radical.

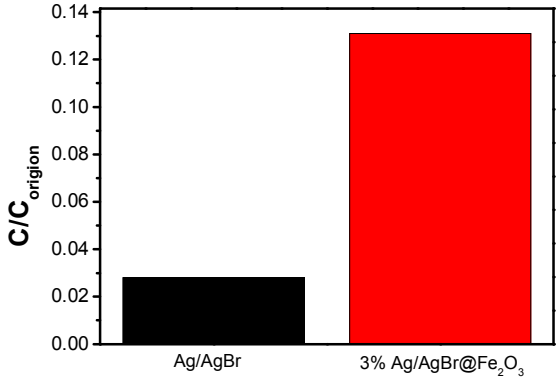

Fig. 14 the MO adsorption results of pure Ag/AgBr and Ag/AgBr@Fe_2O_3 composite in 15 min.

Based on the results of above researches, a possible Z-scheme pathway for the adsorption degradation of MO over Ag/AgBr@Fe_2O_3 was proposed, as shown in Fig. 15, a uniquely hierarchical nanostructure was formed when the Fe_2O_3 nanocrystals were introduced on the surfaces of Ag/AgBr, which would provide a high surface area and numerous active sites for the photocatalytic degradation of organic substances. Under visible light, both Fe_2O_3 and Ag/AgBr were excited. Metallic Ag nanoparticles can absorb visible light, and generated electron−hole pairs.[73] On the one hand, the electrons will transfer to the CB of AgBr or are captured by the O_2 in the solution to form $\bullet O_2^-$.[74,76,77] On the other hand, the remained holes on the metallic Ag nanoparticles will recombine with the electrons that has been excited on the CB of Fe_2O_3 due to the high Schottky barrier at the metal–semiconductor interface.[78] For the VB holes, since the VB of AgBr is 2.6 eV, which is higher than that of the Fe_2O_3 (2.4 eV). So, the holes on the VB of AgBr will transfer to the VB of Fe_2O_3 and directly oxidize organic substances that have been adsorbed in the layer of Fe_2O_3, but neither oxidize OH^- nor H_2O into •OH. In sum, the Fe_2O_3 on the surface of the photocatalysts could improve the adsorbability for organic substances and the interaction between Fe_2O_3, metallic Ag nanoparticles and AgBr greatly improved the separation efficiency of electron−hole pairs and thus enhanced the photocatalytic performance.

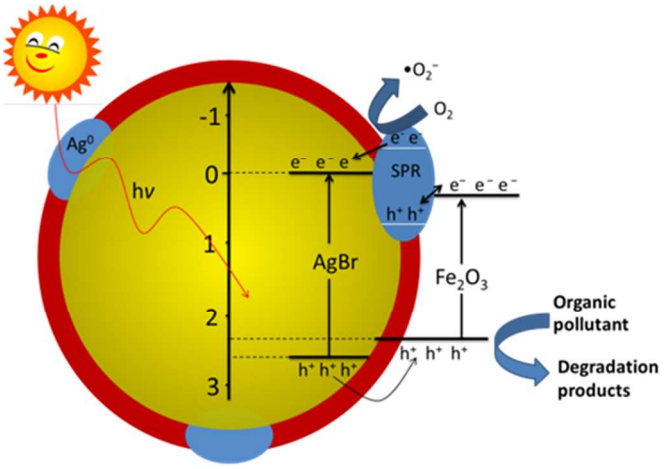

Fig. 15 The proposed mechanism of the reaction process.

4. Conclusions

In summary, Core–shell structured Ag/AgBr@Fe_2O_3 magnetic photocatalyst was prepared successfully via a facile solvothermal process. The Ag/AgBr were covered by Fe_2O_3 and formed a uniquely Core–shell nanostructure, which would provide a high surface area and numerous active sites for the photocatalytic reaction. After the introduction of Fe_2O_3, the Ag/AgBr@Fe_2O_3 composites exhibit increased photocatalytic activity in the degradation of MO and BPA. The 3% Ag/AgBr@Fe_2O_3 composite exhibited the optimal photocatalytic performance. This enhancement could be attributed to the unique CB positions of Fe_2O_3 and Ag/AgBr result in a Z-scheme pathway photocatalytic mechanism, which could improve the separation efficiency of electron−hole pairs.

Furthermore, the Ag/AgBr@Fe_2O_3 composite has antibacterial and magnetic ability, which have greatly extended the applications of Ag/AgBr based photocatalysts.

Acknowledgements

This work is financially supported by the National Natural Science Foundation of China for Youths (No. 21407065), Natural Science Foundation of Jiangsu Province for Youths (BK20140533, BK2012717), China Postdoctoral Science Foundation (No.: 2014M551520, 2014M560399), Jiangsu Postdoctoral Science Foundation (1401143C).

Notes and references

[a] *School of Chemistry and Chemical Engineering, Institute for Energy Research, Jiangsu University, Zhenjiang 212013, PR China*

[b] *Hainan Provincial Key Lab of Fine Chemistry, Hainan University, Haikou, Hainan 570228, P.R. China*

* xh@ujs.edu.cn

1 R. Kumar, S. Anandan, K. Hembram and T. N. Rao, *ACS Appl. Mater. Interfaces*, 2014, **6**, 13138−13148.

2 C. C. Chen, W. H. Ma and J. C. Zhao, *Chem. Soc. Rev*., 2010, **39**, 4206−4219.

3 A. L. Linsebigler, G. Q. Lu and J. T. Yates, *Chem. Rev*., 1995, **95**, 735−758.

4 L. S. Zhang, K. H. Wong, Z. Chen, J. C. Yu, J. C. Zhao, C. Hu, C. Y. Chan and P. K. Wong, *Appl. Catal. A*, 2009, **363**, 221−229.

5 A. Fujishima and K. Honda, *Nature*, 1972, **238**, 37−38.

6 A. Kudo and Y. Miseki, *Chem. Soc. Rev*., 2009, **38**, 253−278.

7 H. Kato ,K. Asakura and A. Kudo, *J. Am. Chem. Soc*., 2003, **125**, 3082−3089.

8 Z. G. Zou, J. H. Ye, K. Sayama and H. Arakawa, *Nature*, 2001, **414** , 625−627.

9 K. Maeda, K. Teramura, D. L. Lu, T. Takata, N. Saito, Y. Inoue and K. Domen, *Nature*, 2006, **440**, 295−295.

10 Z. G. Yi, J. H. Ye, N. Kikugawa, T. Kako, S. X. Ouyang, H. Stuart-Williams, H. Yang, J. Y. Cao , W. J. Luo, Z. S. Li, Y. Liu and R. L. Withers, *Nat. Mater*., 2010, **9**, 559−564.

11 X. B. Chen, S. H. Shen, L. J. Guo and S. S. Mao, *Chem. Rev*., 2010, **110**, 6503−6570.

12 X. B. Chen, L. Liu, P. Y. Yu and S. S. Mao, *Science*, 2011, **331**, 746−750.

13 F. E. Osterloh, *Chem. Mater*. 2008, **20**, 35−54.

14 L. Q. Ye, J. Y. Liu, C. Q. Gong, L. H. Tian, T. Y. Peng and L. Zan, *ACS Catal.*, 2012, **2**, 1677−1683.

15 P. Wang, B. B. Huang, X. Y. Qin, X. Y. Zhang, Y. Dai, J. Y. Wei and M. H. Whangbo, *Angew. Chem. Int. Ed*., 2008, **47**, 7931−7933.

16 P. Wang, B. B. Huang, Z. Lou, X. Zhang, X. Qin, Y. Dai, Z. Zheng and X. Wang, *Chem.−Eur. J*., 2010, **16**, 538−544.

17 P. Wang, B. B. Huang, X. Y. Zhang, X. Y. Qin, H. Jin, Y. Dai, Z. Y. Wang, J. Y. Wei, J. Zhan, S. Y. Wang, J. P. Wang and M. H. Whangbo, *Chem.−Eur. J*., 2009, **15**, 1821−1824.

18 C. An, S. Peng and Y. Sun, *Adv. Mater*., 2010, **22**, 2570−2574.

19 M. S. Zhu, P. L. Chen and M. H. Liu, *ACS Nano*, 2011, **5**, 4529−4536.

20 H. Xu, H. Li, J. Xia, S. Yin, Z. Luo, L. Liu and L. Xu, *ACS Appl. Mater. Interfaces*, 2011, **3**, 22−29.

21 Y. Y. Li and Y. Ding, *J. Phys. Chem. C*, 2010, **114**, 3175−3179.

22 Y. F. Shen, P. L. Chen, D. Xiao, C. C. Chen, M. S. Zhu, T. S. Li, W. G. Ma and M. H. Liu, *Langmuir*, 2015, **31**, 602–610.

23 B. Li, H. Wang, B. W. Zhang, P. F. Hu, C. Chen and L. Guo, *ACS Appl. Mater. Interfaces*, 2013, **5**, 12283–12287.

24 H. X. Shi, G. S. Li, H. W. Sun, T. C. An, H. J. Zhao and P. K. Wong, *Appl. Catal. B: Environ*., 2014, **158**, 301–307.

25 H. Tong, S. X. Ouyang, Y. P. Bi, N. Umezawa, M. Oshikiri and J. H. Ye, *Adv. Mater*., 2012, **24**, 229–251.

26 W. B. Hou and S. B. Cronin, *Adv. Funct. Mater*., 2013, **23**, 1612–1619.

27 Z. Z. Lou, Z. Y. Wang, B. B. Huang and Y. Dai, *ChemCatChem*., 2014, **6**, 2456–2476.

28 B. Z. Tian, R. F. Dong, J. M. Zhang, S. Y. Bao, F. Yang and J. L. Zhang, *Appl. Catal. B: Environ*., 2014, **158**, 76–84.

29 P. Wang, B. B. Huang, Y. Dai and M. H. Whangbo, *Phys. Chem. Chem. Phys*., 2012, **14**, 9813–9825.

30 B. Z. Tian and J. L. Zhang, *Catal. Surv. Asia*, 2012, **16**, 210–230.

31 B. Z. Tian, T. T. Wang, R. F. Dong, S. Y. Bao, F. Yang and J. L. Zhang, *Appl. Catal. B: Environ*., 2014, **147**, 22– 28.

32 J. F. Guo, B. W. Ma, A. Y. Yin, K. N. Fan and W. L. Dai, *Appl. Catal. B: Environ*., 2011, **101**, 580–586.

33 C. H. An, X. J. Ming, J. Z. Wang and S. T. Wang, *J. Mater. Chem*., 2012, **22**, 5171-5176.

34 Y. G. Xu, T. Zhou, S. Q. Huang, M. Xie, H. P. Li, H. Xu, J. X. Xia and H. M. Li, *RSC Adv*., 2015, **5**, 41475–41483.

35 S. Yang, Y. Y. Xu, Y. Q. Sun, G. Y. Zhang and D. Z. Gao, *CrystEngComm*, 2012, **14**, 7915–7921

36 X. S. Zhang, H. C. Li, S. J. Wang, Fu-Ren F. Fan and A. J. Bard, *J. Phys. Chem. C*, 2014, **118**, 16842−16850.

37 Y. J. Lin, S. Zhou, S.W. Sheehan and D.W. Wang, *J. Am. Chem. Soc*., 2011, **133**, 2398–2401.

38 B. Klahr, S. Gimenez, F. F. Santiago, T. Hamann and J. Bisquert, *J. Am. Chem. Soc*., 2012, **134**, 4294–4302.

39 J. H. Kennedy and K.W. Frese, *J. Electrochem. Soc*., 1978, **125**, 709–714.

40 L. L. Peng, T. F. Xie, Y. C. Lu, H. M. Fan and D. J. Wang, *Phys. Chem. Chem. Phys*., 2010, **12**, 8033–8041.

41 W. Wu, S. F. Zhang, X. H. Xiao, J. Zhou, F. Ren, L. L. Sun and C. Z. Jiang, *ACS Appl. Mater. Interfaces*, 2012, **4**, 3602−3609.

42 Y. Shi, H. Y. Li, L. Wang , W. Shen and H. Z. Chen, *ACS Appl. Mater. Interfaces*, 2012, **4**, 4800−4806

43 S. Ye, L. G. Qiu, Y. P. Yuan, Y. J. Zhu, J. Xia and J. F. Zhu, *J. Mater. Chem. A*, 2013, **1**, 3008–3015.

44 J. Wang, C. An, J. Liu, G. Xi, W. Jiang, S. Wang and Q. H. Zhang, *J. Mater. Chem. A*, 2013, **1**, 2827−2832.

45 Y. H. Yan, H. Y. Guan, S. Liu and R. Y. Jiang, *Ceram. Int*., 2014, **40**, 9095–9100.

46 J. X. Liu, D. F. Zhang, X. P. Pu, D. Y. Dong, P. Q. Cai and H. J. Seo, *Mater. Lett*., 2014, **130**, 94–96.

47 J. Di, J.X. Xia, S. Yin, H. Xu, M.Q. He, H.M. Li, L. Xu and Y. P. Jiang, *RSC Adv*., 2013, **3**, 19624–19631.

48 Y. G. Xu, H. Xu, J. Yan, H. M. Li, L. Y. Huang, Q. Zhang, C. J. Huang and H. L. Wan, *Phys. Chem. Chem. Phys*., 2013, **15**, 5821–5830.

49 Y. G. Xu, M. Xie, T. Zhou, S. Yin, H. Xu, H. Y. Ji, H. M. Li and Q. Zhang, *New J. Chem*., 2015,**39**, 5540-5547.

50 P. Wang, B. B. Huang, Q. Q. Zhang, X. Y. Zhang, X. Y. Qin, Y. Dai, J. Zhan, J. X. Yu, H. X. Liu and Z. Z. Lou, *Chem.−Eur. J*., 2010, **16**, 10042–10047.

51 Y. G. Xu, H. Xu, J. Yan, H.M. Li, L.Y. Huang, J.X. Xia, S. Yin and H.M. Shu, *Colloids Surf. A: Physicochem. Eng. Aspects*, 2013, **436**, 474–483.

52 S. L. Lin, L. Liu, J. S. Hu, Y. H. Liang and W. Q. Cui, *Appl. Surf. Sci*., 2015, **324**, 20–29.

53 X. N. Liu, Q. F. Lu, C. F. Zhua and S. W. Liu, *RSC Adv*., 2015, **5**, 4077–4082.

54 S. Q. Huang, Y. G. Xu, M. Xie, H. Xu, M. Q. He, J. X. Xia, L. Y. Huang and H. M. Li, *Colloids Surf. A: Physicochem. Eng. Aspects*, 2015, **478**, 71–80.

55 S. K. Maji, N. Mukherjee, A. Mondal and B. Adhikary, *Polyhedron*, 2012, **33**, 145–149

56 J. Di, J. X, Xia, S. Yin, H. Xu, L. Xu, Y. G. Xu, M. Q. He and H. M. Li, *J. Mater. Chem. A*, 2014, **2**, 5340–5351.

57 Y. Sang, L. Kuai, C. Y. Chen, Z. Fang and B. Y. Geng, *ACS Appl. Mater. Interfaces*, 2014, **6**, 5061−5068.

58 Y. Zhang, J. Gu, M. Murugananthan, Y. R. Zhang, *J. Alloys. Compd*., 2015, **630**, 110–116.

59 H. Xu, J. Yan, Y. G. Xu, Y. H. Song, H. M. Li, J. X. Xia, C. J. Huang and H. L. Wan, *Appl. Catal. B: Environ*., 2013, **129**, 182–193.

60 Y. Hou, F. Zuo, A. Dagg and P. Y. Feng, *Nano Lett*. 2012, **12**, 6464−6473

61 Y. G. Xu, M. Xie, S. Q. Huang, H. Xu, H. Y. Ji, J. X. Xia, Y. P. Li and H. M. Li, *RSC Adv*., 2015, **5**, 26281-26290.

62 Q. Xiang, J. Yu and M. Jaroniec, *J. Phys. Chem. C*, 2011, **115**, 7355–7363.

63 J. Jiang, X. Zhang, P. B. Sun and L.Z. Zhang, *J. Phys. Chem. C*, 2011, **115**, 20555–20564.

64 L. Z. Dong, Y. M. He, T. T. Li, J. Cai, W. D. Hu, S. S. Wang, H. J. Lin, M. F. Luo, X. D. Yi, L. H. Zhao, W. Z. Weng and H. L. Wan, *Appl. Catal. A*, 2014, **472**, 143−151.

65 Y. P. Bi, S. X. Ouyang, J. Y. Cao and J. H. Ye, Phys. *Chem. Chem. Phys*. 2011, **13**, 10071−10075.

66 Y. J. Wang, Z. X. Wang, S. Muhammad and J. He, *CrystEngComm*., 2012, **14**, 5065−5070.

67 X. L. Xiao, L. Ge, C. C. Han, Y. J. Li, Z. Zhao, Y. J. Xin, S. Fang, L. Wu and P. Qiu, *Appl. Catal. B: Environ*., 2015, **163**, 564–572.

68 P. H Li, B. L. Li, Z. M. An, L. P. Mo, Z. S. Cui and Z. H. Zhang, *Adv. Synth. Catal*. 2013, **355**, 2952–2959

69 X. Xiao, R. Hao, M. Liang, X. X. Zuo, J. Nan, L. S. Li, W. D. Zhang, *J. Hazard. Mater*., 2012, **233**, 122–130.

70 X. J. Bai, L. Wang, Y. J. Wang, W. Q. Yao, Y. F. Zhu, *Appl. Catal. B: Environ*., 2014, **152**, 262–270.

71 J. G. Yu and B. Wang, *Appl. Catal. B: Environ*., 2010, **94**, 295–302.

72 G. D. Yang, Z. Jiang,H. H. Shi, T. C. Xiao and Z. F. Yan, *J. Mater. Chem*., 2010, **20**, 5301–5309.

73 S. Linic, P. Christopher and D. B. Ingram, *Nature Mater*., 2011, **10**, 911−921.

74 H. F. Cheng, B. B. Huang, P. Wang, Z. Y. Wang, Z. Z. Lou, J. P. Wang, X. Y. Qin, X. Y. Zhang and Y. Dai, *Chem. Commun*., 2011, **47**, 7054−7056.

75 X. F. Zhou, C. Hu, X. X. Hu, T. W. Peng and J. H. Qu, *J. Phys. Chem. C*, 2010, **114**, 2746−2750.

76 J. Di, J. X. Xia, Y. P. Ge, H. P. Li, H. Y. Ji, H. Xu, Q. Zhang, H. M. Li, M. N. Li, *Appl. Catal. B: Environ.*, 2015, **168**, 51–61.

77 C.C. Shen, Q. Zhu, Z. W. Zhao, T. Wen, X. K. Wang and A. W. Xu, *J. Mater. Chem. A*, 2015, Advance Article.

78 H. G. Yu, R. Liu, X. F. Wang, P. Wang and J. G. Yu, *Appl. Catal. B: Environ*., 2012,**111**, 326−333.

79 Y. H. Liang, S. L. Lin, L. Liu, J. S. Hu, W. Q. Cui, *Appl. Catal. B: Environ*., 2015, **164**, 192–203.

80 (a) M. S. A. S. Shah, W. Kim, J. Park, D. K. Rhee, I. H. Jang, N. G. Park, J. Y. Lee and P.J. Yoo, *ACS Appl. Mater. Interfaces*, 2014, **6**, 20819−20827; (b) J. Tian, R. Liu, G. H. Wang, Y. Xu, X. Wang and H. Yu, *Appl. Surf. Sci.*, 2014, **319**, 324–331; (c) C. Dong, K. L. Wu, X. W. Wei, J. Wang, Li Liu and B. B. Jiang, *Appl. Catal. A: Gen.*, 2014, **488**, 11–18; (d) H. Xu, H. M. Li, J. X. Xia, S. Yin, Z. J. Luo, L. Liu and L. Xu, *ACS Appl. Mater. Interfaces*, 2011, **3**, 22–29.

